Journal of Alloys and Compounds 689 (2016) 87–93

Contents lists available at ScienceDirect

Journal of Alloys and Compounds

journal homepage: http://www.elsevier.com/locate/jalcom

Enhanced thermoelectric performance of highly oriented polycrystalline SnSe based composites incorporated with SnTe nanoinclusions

Haifeng Guo, Hongxing Xin*, Xiaoying Qin**, Jian Zhang, Di Li, Yuanyue Li, Chunjun Song, Cong Li

Key Laboratory of Materials Physics, Institute of Solid State Physics, Chinese Academy of Sciences, 230031 Hefei, People's Republic of China

ARTICLE INFO

Article history:
Received 17 March 2016
Received in revised form
19 July 2016
Accepted 26 July 2016
Available online 28 July 2016

Keywords:
Tin selenide
Nano-structured tin tellurium
Nano-composite
Thermoelectric performance

ABSTRACT

Binary single crystal compound SnSe with high thermoelectric performance has drawn great attention to polycrystalline SnSe. Here, we synthesized highly oriented p-type polycrystalline composite samples *f* mol% SnTe/$Ag_{0.005}Sn_{0.995}Se$ ($f = 0$, 0.5, 1 and 1.5) and present thermoelectric performance from 300 K to 900 K. High thermoelectric figure of merit (*ZT*) of the matrix $Ag_{0.005}Sn_{0.995}Se$ should be attributed to highly oriented crystal grains along the (400) plane. Moreover, proper proportional ($f = 0.5$) incorporation of SnTe nanoinlusions into $Ag_{0.005}Sn_{0.995}Se$ matrix enhances the power factor and reduces lattice thermal conductivity, which could be due to the contribution of enhanced phonon scattering resulting from abundant interfaces. Consequently, a largest *ZT* value of 1.6 ± 0.2 is achieved at 875 K for composite sample 0.5 mol% SnTe/$Ag_{0.005}Sn_{0.995}Se$. Furthermore, these polycrystalline composites have large values of *ZT* (>1) from 800 K to 900 K and good experimental repeatability, which suggests that it is a promising candidate for high temperature power generation.

1. Introduction

Thermoelectric (TE) materials provide a means of direct electrical power generation from sources of heat, making them particularly appealing in clean energy, refrigeration and energy harvesting fields. The efficiency of a thermoelectric material is estimated with the dimensionless figure of merit: $ZT = S^2T/\rho(\kappa_l + \kappa_e)$, where *S*, *T*, ρ, κ_e, κ_l are the Seebeck coefficient (or thermopower), absolute temperature, resistivity, electron thermal conductivity and lattice thermal conductivity, respectively [1–3]. In order to acquire high ZT, power factor ($PF = S^2/\rho$) must be enlarged, and meanwhile resistivity and thermal conductivity should be minimized.

Recently, an investigation pointed out that binary single crystal compound SnSe possessed unprecedented high ZT of 2.6 ± 0.3 at 923 K along the b axis of the room-temperature orthorhombic unit cell, being attributed to the ultralow lattice thermal conductivity due to the large lattice anharmonicity and anisotropic layered structure [4]. Despite all that, considering the high cost and difficult preparation method of single crystal SnSe [4–6], polycrystalline SnSe is much more available than single crystal SnSe in practical large-scale applications. Therefore, much attention has been paid to optimization of polycrystalline based SnSe. Because stoichiometric SnSe shows high resistivity and low carrier density (~10^{17} cm^{-3}), chemical doping is reasonably applied in tuning carrier density and optimizing thermoelectric performance. For example, the peak ZT is 0.6 at 750 K for the Ag-doped polycrystalline SnSe [7] and similarly 0.72 at 750 K for the Na, Te-codoped polycrystalline SnSe [8]. Up to now, however, the reported *ZT* values of polycrystalline SnSe are not larger than unit in the temperature range from 300 K to 780 K. Hence, it is highly urgent and significant to enhance the thermoelectric performance of SnSe based poly-crystals. Moreover, in spite of great efforts to optimize thermoelectric performance of polycrystalline SnSe, the strategy by fabricating SnSe based polycrystalline bulk with highly preferred orientation along the b axis of single crystal SnSe has not been reported until now. On the other hand, incorporating nano-sized particles into polycrystalline SnSe based system to enhance ZT has also scarcely been reported. Considering the successful application of this strategy in PbTe-and

* Corresponding author.
** Corresponding author.
E-mail addresses: xinhongxing@issp.ac.cn (H. Xin), xyqin@issp.ac.cn (X. Qin).

http://dx.doi.org/10.1016/j.jallcom.2016.07.291
0925-8388/

Bi_2Te_3-based compounds [9–12], one can expect that it could be a feasible method to elevate thermoelectric performance of polycrystalline SnSe based system.

The present work was conducted with two motivations to enhance thermoelectric performance of polycrystalline SnSe based system: one is to synthesize bulk matrix $Ag_{0.005}Sn_{0.995}Se$ with highly preferred orientation by solid solution with a special cooling technique. The other one is both to reduce the resistivity of polycrystalline SnSe by Ag-doping and to reduce the lattice thermal conductivity by incorporating with nanophase SnTe. Here, we synthesized highly oriented p-type polycrystalline composite samples *f* mol% SnTe/$Ag_{0.005}Sn_{0.995}Se$ (f = 0, 0.5, 1 and 1.5) and present thermoelectric performance from 300 K to 900 K $Ag_{0.005}Sn_{0.995}Se$ shows p-type conductive behavior with high carrier density on the order of 10^{18} cm^{-3}, which can be ascribed to that extra holes introduced by substituting Sn with Ag. Moreover, $Ag_{0.005}Sn_{0.995}Se$ possesses ultralow lattice thermal conductivity close to that of pristine SnSe [4] On the other hand, SnTe is a highly degenerate p-type semiconductor with high hole concentration (~10^{21} cm^{-3}) arising from the inherent Sn deficiency in the lattice and shows high electrical and thermal conductivity [13,14]. Indeed, our results indicate that incorporation of 0.5 mol% of SnTe results in ~9% increase in *PF* and ~12% decrease in κ_l at 875 K, leading to a largest *ZT* of 1.6 ± 0.2. Furthermore, the obtained materials have large values of *ZT* (>1) in the temperature range from 800 K to 900 K, which suggests that it is a promising candidate for high temperature power generation.

2. Experimental section

Commercial elemental Ag (99.99%), Sn (99.99%), Se (99.99%) powders were weighed according to the stoichiometry as starting materials. The powder mixtures were loaded into a clean evacuated quartz ampoule pumped under vacuum of 10^{-3} Pa and melted using a vertical dual-zone furnace at 1223 K for 24 h. In order to obtain the bulk matrix with highly preferred orientation, the lower side of quartz ampoule was first cooled down to 1123 K with a rate of 0.2 K/min while the upper side of quartz ampoule was kept at 1223 K. Then, the whole quartz ampoule began cooling down to 573 K with a rate of 1 K/min, and then cooled to room temperature. Then, the ingots were mechanically powdered by mortar and pestle and sieved to <50 μm. On the other hand, to synthesize SnTe nanopowders with the nominal composition, 15 g NaOH and 5 g $NaBH_4$ were put into a 1000 ml glass beaker containing 600 ml deionized water, and then 200 ml anhydrous ethylenediamine was put into the beaker; the solution was stirred by a magnetic stirrer at room temperature. Then, 50 mmol Te (99.99%) and 50 mmol $SnCl_2$ were added into the solution. The solution was then heated to 423 K on the oil bath and meanwhile stirred by a magnetic stirrer at the speed of 1700 r/s. After about 2 h, a large quantity of particles was precipitated. Then, the precipitates were collected, filtered and washed respectively with anhydrous ethanol and distilled water until a pH value close to 7 was obtained, and then dried under vacuum at 353 K for 10 h. The SnTe nanopowders thus obtained and $Ag_{0.005}Sn_{0.995}Se$ powders were mixed in a planetary mill for 2 h in accordance with the molar ratios of 0.5:99.5, 1:99 and 1.5:98.5. The bulk nano-composite samples with disk-shaped pellets (20 mm in diameter) were obtained by using spark plasma sintering (SPS), where 20 MPa of axial pressure was applied for 10 min at 673 K under a pulsed electric current in an argon atmosphere.

The phase structure of all samples was examined by X-ray diffraction (XRD) using Ni-filtered Cu Kα radiation operating at 40 kV and 40 mA. The morphologies and fractographs of the samples were observed by field emission scanning electron microscopy (FE-SEM) equipped with a detector for energy dispersive X-ray spectroscopy (EDS). The transmission electron microscopy (TEM) observations were carried out using a JEM-2010 operating at 200 kV. Electrical resistivity and Seebeck coefficient were measured by the ZEM-3 system from ULVAC under Helium atmosphere from 300 to 900 K. The measurement error is ±5% for Seebeck coefficient and ±5% for resistivity. The thermal diffusivity *D* was measured using the laser flash method (Netzsch, LFA-457). It should be pointed out that due to the anisotropic characteristic of SnSe alloys, *D* is measured along the direction normal to the pressing direction, ensuring that the thermal and electrical properties are measured in the same direction. The specific heat of the composite samples was determined by a weighted average of the temperature-dependent specific heat literature values for $Ag_{1-x}Sn_xSe$ and SnTe [7,18]. The density *d* was determined to be around 6.07 g/cm^3 for all samples (see Table S1). The density values of all samples measured by Archimedes' methods using alcohol as the medium were greater than 98% theoretical density (6.19 g/cm^3). Total thermal conductivity (with the error of ±5%) was calculated from $\kappa_{tot} = DdC_p$, where *D* is the thermal diffusivity, C_p is the heat capacity, and d is the mass density of the specimens. The uncertainty of *ZT* is around ±10%. The room temperature (300 K) Hall coefficients were measured using the physical property measurement system (PPMS) in the magnetic fields ranging from 0 to 3 T and then carrier concentrations were calculated from the Hall data.

3. Results and discussions

3.1. Microstructure characteristics

The XRD patterns of SnTe nanopowders and bulk composite samples *f* mol% SnTe/$Ag_{0.005}Sn_{0.995}Se$ (f = 0, 0.5, 1 and 1.5) are shown in Fig. 1. The main diffraction peaks match well with the standard JCPDS cards (SnSe: No.01-089-0234, SnTe: No.03-065-0308). Clearly, all of the bulk samples *f* mol% SnTe/$Ag_{0.005}Sn_{0.995}Se$ (f = 0, 0.5, 1 and 1.5) show highly preferred orientation along the (400) plane. The (400) plane orientation factor of SPS processed bulk samples $Ag_{0.005}Sn_{0.995}Se$ is 0.61 (see Table S1). The (400) plane orientation factors of bulk composite samples *f* mol% SnTe/$Ag_{0.005}Sn_{0.995}Se$ (f = 0.5, 1 and 1.5) are smaller than that of sample $Ag_{0.005}Sn_{0.995}Se$, probably because their

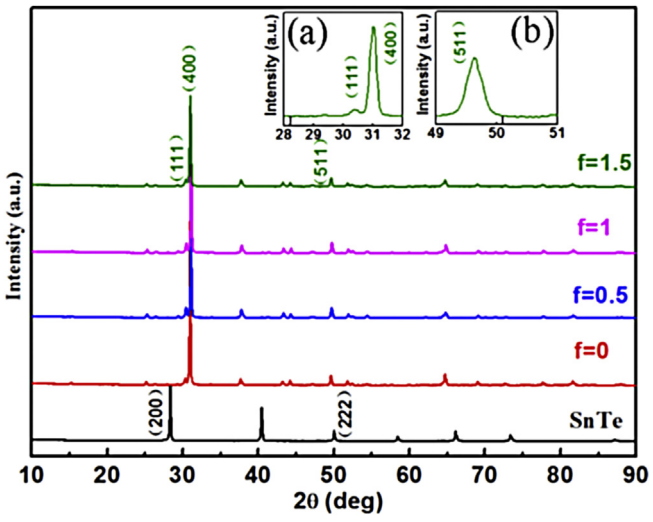

Fig. 1. XRD patterns for co-precipitation synthesized SnTe nanopowders and SPS synthesized bulk samples *f* mol% SnTe/$Ag_{0.005}Sn_{0.995}Se$ (f = 0, 0.5, 1 and 1.5). The inset **(a)** and **(b)** show the amplification of the stronger diffraction peak (400), (111) and (511) of XRD patterns for 1.5 mol% SnTe/$Ag_{0.005}Sn_{0.995}Se$.

preferential grain growth is suppressed when incorporating SnTe nanoparticles. Moreover, the inset **(a)** and **(b)** depict the amplification of the stronger diffraction peak (400), (111) and (511) in the bulk composite sample 1.5 mol% SnTe/$Ag_{0.005}Sn_{0.995}Se$. One can see that the typical peaks (200) and (222) of SnTe were not observed in the composite sample presumably due to its relatively lower concentration. Actually, our FE-SEM and TEM observations confirmed the existence of SnTe (see the following text).

Fig. 2(a) shows the FE-SEM images for co-precipitation synthesized SnTe nanopowders. One can observe that SnTe has smaller particle size in 50–600 nm and some larger particle size in 1–1.5 μm. In details, the particle size distribution of the SnTe powders is shown in Fig. 2(b). It can be seen that the average particle size of SnTe powders is around 550 nm. Fig. 3(a) shows the fracture surface of solid-melting bulk sample $Ag_{0.005}Sn_{0.995}Se$. It can be seen that $Ag_{0.005}Sn_{0.995}Se$ behaves a highly preferred orientation and a dense microstructure being composed of lamella with a thickness of 1–2.5 μm. Fig. 3(b) shows the fracture surface of SPS processed bulk sample 1.5 mol% SnTe/$Ag_{0.005}Sn_{0.995}Se$. One can see that the average particle size of SPS processed bulk samples is around 10 μm. Clearly, the milling and SPS process destroy partly the orientation of solid-melting $Ag_{0.005}Sn_{0.995}Se$, and the grain-orientation distribution of SPS processed bulk samples manifested long-range disorder and short-range order. Moreover, considering the anisotropy of $Ag_{0.005}Sn_{0.995}Se$, we measured the electrical properties along the direction perpendicular to the pressing direction and measured the thermal properties along the direction normal to the pressing direction in this work.

To confirm the existence of SnTe phase, TEM observations were performed. Fig. 4(a) and (b) give the low magnificent bright-field TEM images of SPS processed bulk composite sample 1.5 mol% SnTe/$Ag_{0.005}Sn_{0.995}Se$. We conducted a lot of observations by focusing on the surface of composite sample 1.5 mol% SnTe/$Ag_{0.005}Sn_{0.995}Se$, and two typical morphologies in the bulk composite sample were found. Later analysis confirmed that one is the characteristic morphology of $Ag_{0.005}Sn_{0.995}Se$ along the (111) plane and the other is SnTe phase. Fig. 4(c) shows the lattice image of $Ag_{0.005}Sn_{0.995}Se$ preferred orientation along the (400) and (111) plane (corresponding to the rectangle area A in Fig. 4(a)). It can be seen that a minority of SnSe preferred orientation along the (111) plane appear in the main matrix $Ag_{0.005}Sn_{0.995}Se$ preferred orientation along the (400) plane, resulting in the short-range disordered lattices. Fig. 4(d) gives the lattice image of $Ag_{0.005}Sn_{0.995}Se$ preferred orientation along the (400) plane and nanophase SnTe (corresponding to the circular area B in Fig. 4(a)). Clearly, a phase boundary between the $Ag_{0.005}Sn_{0.995}Se$ matrix (the upper side) and SnTe inclusion (the lower side) can be seen. By careful inspection with EDS for the circular area B in Fig. 4(a), one can see from Fig. 4(e) that the observed dark particles in Fig. 4(b) contain element Te. Furthermore, as shown in Fig. 4(f), the electron diffraction pattern along the [001] direction of the observed dark particles in Fig. 4(b) can be readily indexed to the SnTe structure at the room temperature, in good agreement with observations with EDS as shown in Fig. 4(e). Present results indicate that SnTe nanoparticles were successfully incorporated into the $Ag_{0.005}Sn_{0.995}Se$ matrix, forming nanocomposite samples SnTe/$Ag_{0.005}Sn_{0.995}Se$.

3.2. Electrical transport properties

Fig. 5 depicts the electrical resistivity ρ **(a)**, Seebeck coefficient S **(b)**, and power factor **(c)** of SPS processed bulk composite samples f mol% SnTe/$Ag_{0.005}Sn_{0.995}Se$ ($f = 0, 0.5, 1$ and 1.5). For all the samples, ρ shows the same temperature-dependent trend. Firstly, ρ manifests a doped semiconductor behavior with the electrical resistivity increasing as temperature increases at low temperatures (300 K–550 K); Secondly, ρ decreases with increasing temperature at middle temperatures (550 K–800 K), being attributed to the thermal activation of charge carriers. Then, ρ slightly increases above 800 K. This trend could be due to the easier activation of minority carriers across the smaller band gap in the high-temperature phase, which is consistent with the phase transition from Pnma (0.61 eV) to the Cmcm (0.39 eV) space group. Furthermore, Fig. 5(a) shows that ρ increases from 11.4 mΩ*cm to 17.2 mΩ*cm, 22.2 mΩ*cm and 22.8 mΩ*cm, as f increase from 0 to 0.5, 1 and 1.5 at 300 K. It can be seen that ρ of all the composite samples at 300 K are higher than that of pristine $Ag_{0.005}Sn_{0.995}Se$ probably due to enhancement of carrier scattering caused by SnTe addition.

The temperature dependencies of S are shown in Fig. 5(b). S values for all the samples are positive, indicating that they belong to typical p-type semiconductor. Moreover, S values of all the composite samples are higher than that of pristine $Ag_{0.005}Sn_{0.995}Se$, which is similar to that of ρ for all the samples. One can see that S values increase from 261 μV/K to 288 μV/K and then to 323 μV/K, as f increase from 0 to 0.5 and 1 at 300 K. The decrease of S values above 550 K is consistent with the decreasing trend of electrical resistivity, suggesting that mixture conduction process works. The upturn of S values above 800 K could be due to the phase transition from Pnma (0.61 eV) to the Cmcm (0.39 eV) space group [4].

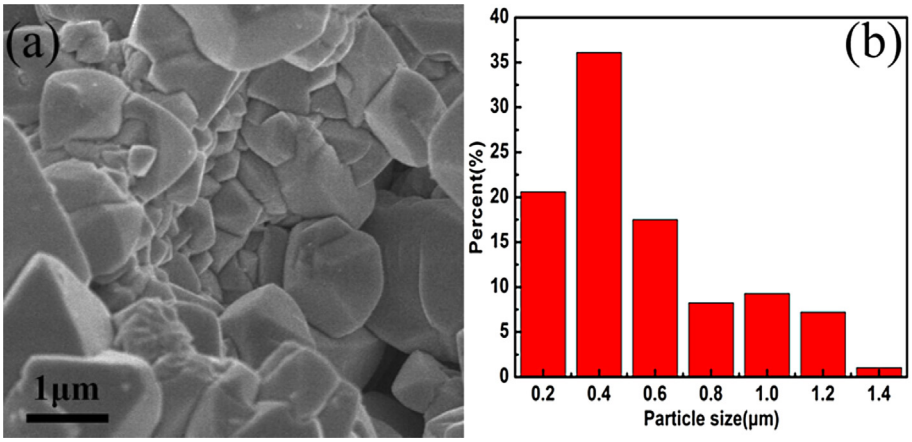

Fig. 2. **(a)** SEM images for co-precipitation synthesized SnTe nanopowders and **(b)** the particle size distribution of co-precipitation synthesized SnTe powders.

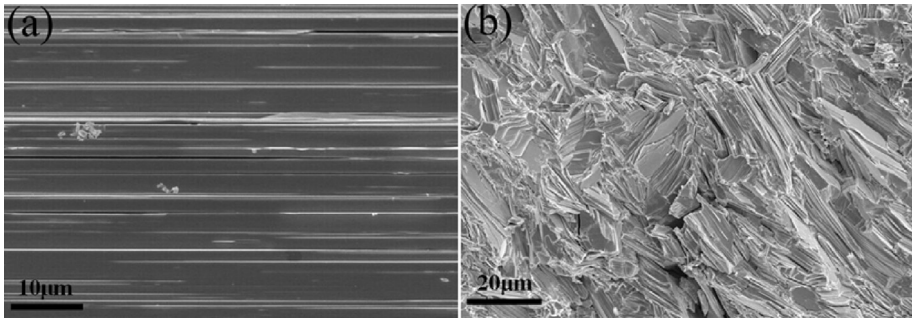

Fig. 3. SEM images for the fracture surface of **(a)** solid-melting bulk sample $Ag_{0.005}Sn_{0.995}Se$ and **(b)** SPS processed bulk composite sample 1.5 mol% SnTe/$Ag_{0.005}Sn_{0.995}Se$.

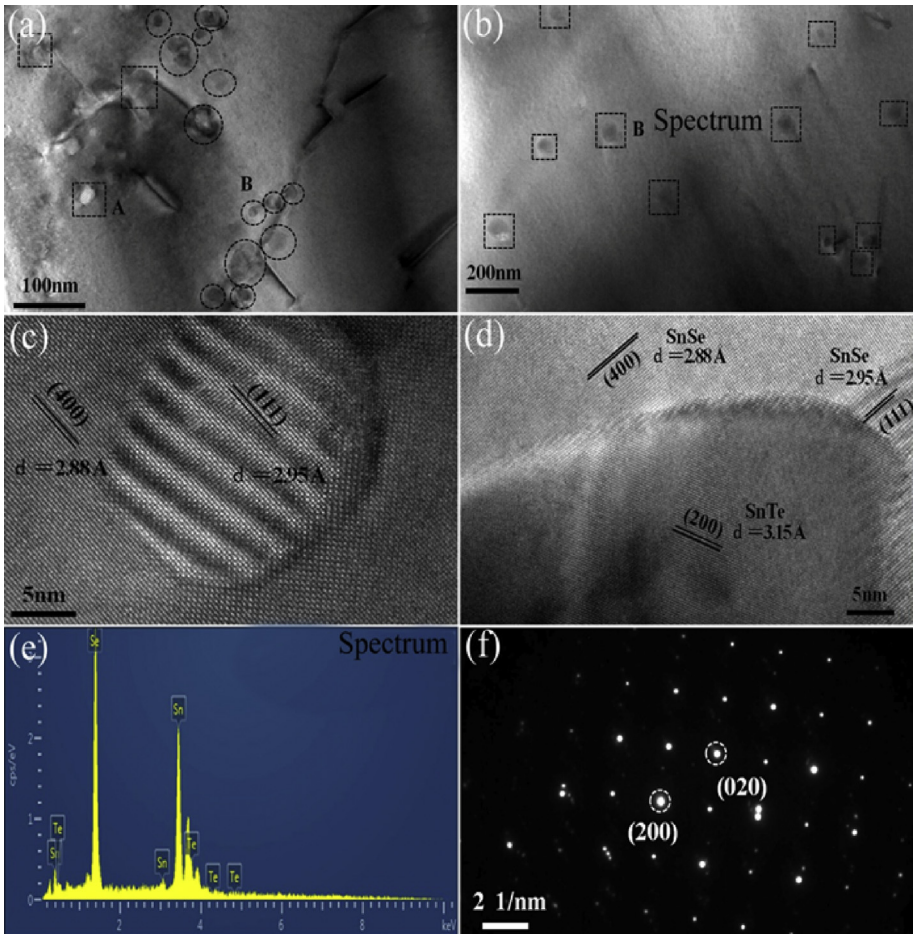

Fig. 4. **(a)** and **(b)** give low magnificent bright-field TEM images of SPS processed bulk sample 1.5 mol% SnTe/$Ag_{0.005}Sn_{0.995}Se$; **(c)** the lattice image of SnSe preferred orientation along the (400) and (111); **(d)** the lattice image of SnSe preferred orientation along (400) and nanophase SnTe; **(e)** EDS patterns detected in the marked area B in (b); **(f)** electron diffraction pattern along [001] direction of the observed dark particles in the marked area B in (b).

Moreover, the enhanced high temperature Seebeck coefficient (800 K–850 K) is probably due to the heavy band contribution of SnTe [13].

In order to understand the behavior of ρ and S, the room temperature hole carrier concentration p is determined, as given in Table 1 that also lists the room-temperature electrical resistivity ρ, Seebeck coefficient S, and hole mobility μ of SPS processed bulk composite samples f mol% SnTe/$Ag_{0.005}Sn_{0.995}Se$ (f = 0, 0.5, 1 and 1.5). All of the composite samples show p-type conduction behavior with carrier density being in the order of 10^{18} cm^{-3}, and in details carrier concentration p decreases from 6.52 × 10^{18} cm^{-3} to 3.99 × 10^{18} cm^{-3} and 3.66 × 10^{18} cm^{-3}, as f increase from 0 to 0.5 and 1, respectively. One can see that ρ increases with increasing SnTe content f (except f = 1.5). Based on the relation $\rho = (pe\mu)^{-1}$, the increase in ρ of the composite samples f mol% SnTe/$Ag_{0.005}Sn_{0.995}Se$ (f = 1 and 1.5) result from the decreased hole carrier concentration and mobility. Specially, it can be seen clearly that the slight increase in ρ of the composite sample 0.5 mol% SnTe/$Ag_{0.005}Sn_{0.995}Se$ results from the heavily decreased carrier concentration p. Similarly, the slight increase in μ of the composite sample 0.5 mol% SnTe/$Ag_{0.005}Sn_{0.995}Se$ could be due to the obvious decrease in p. In contrast, decreased mobility of the composite samples f mol% SnTe/

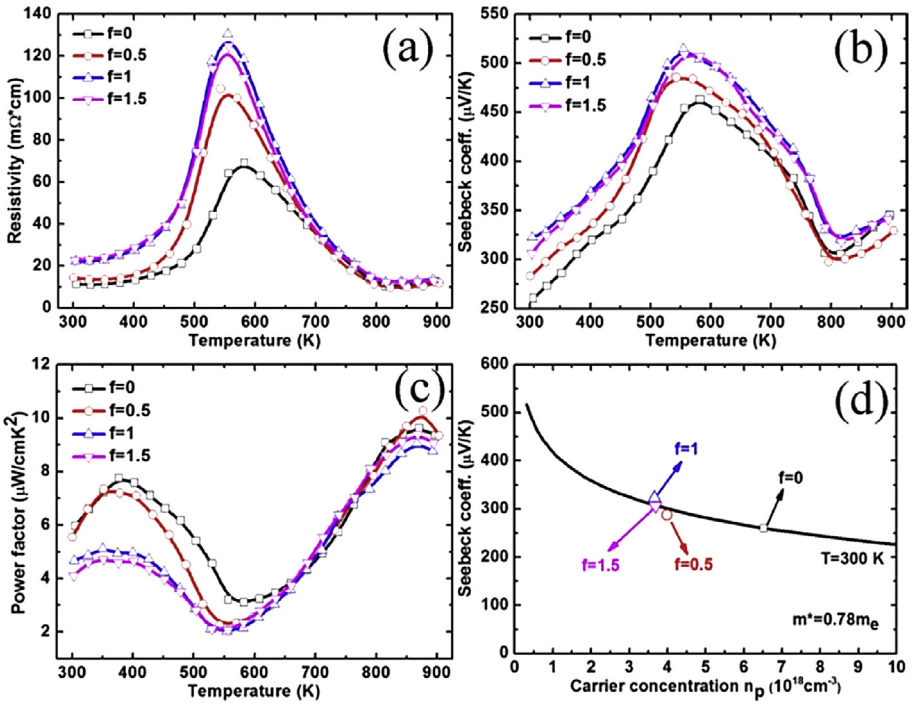

Fig. 5. **(a)**Electrical resistivity, **(b)** Seebeck coefficient and **(c)** Power factor as a function of temperature for SPS synthesized bulk samples *f* mol% SnTe/$Ag_{0.005}Sn_{0.995}Se$ ($f = 0$, 0.5, 1 and 1.5); **(d)** A Pisarenko plot of the Seebeck coefficient as a function of hole carrier concentration for the composite samples at 300 K.

Table 1
List of electrical resistivity ρ, Seebeck coefficient S, carrier concentration p and Hall mobility μ at room temperature (300 K) for *f* mol% SnTe/$Ag_{0.005}Sn_{0.995}Se$ ($f = 0$, 0.5, 1 and 1.5).

f mol% SnTe/$Ag_{0.005}Sn_{0.995}Se$	ρ (mΩ*cm)	S (μV/K)	P (10^{18} cm^{-3})	μ (cm^2 V^{-1} s^{-1})
0	11.4	261	6.52	84.4
0.5	17.2	288	3.99	90.9
1	22.2	323	3.66	76.9
1.5	22.8	306	3.68	74.4

$Ag_{0.005}Sn_{0.995}Se$ ($f = 1$ and 1.5) is probably due to the enhanced interface scattering from the increased SnTe nanoparticles. In addition, Seebeck coefficient of a degenerate semiconductor can be expressed by the Mott formula (1) [15]:

$$S = \frac{\pi^2 k_B^2 T}{3q}\left(\frac{\partial \ln(\sigma(E))}{\partial E}\right)_{E=E_f} = \frac{\pi^2 k_B^2 T}{3q}\left[\frac{1}{p}\frac{\partial p(E)}{\partial E} + \frac{\partial \mu(E)}{\partial E}\right]_{E=E_f} \quad (1)$$

where q, k_B, E_f are the carrier charge, the Boltzmann constant, and the Fermi energy, respectively. Formula (1) indicates that S increases with decreasing p which can explain qualitatively why S of samples *f* mol% SnTe/$Ag_{0.005}Sn_{0.995}Se$ ($f = 0$, 0.5 and 1) increase with increasing *f*. It is worthwhile to notice that S value of sample 1 mol% SnTe/$Ag_{0.005}Sn_{0.995}Se$ is slightly larger than that of 1.5 mol% SnTe/$Ag_{0.005}Sn_{0.995}Se$ (see Table 1). Therefore, a Pisarenko plot of the Seebeck coefficient as a function of carrier concentration is shown in Fig. 5(d) together with the theoretical line calculated based on simple parabolic band model for p-type $Ag_{0.005}Sn_{0.995}Se$. Based on simple parabolic band modelling, the effective mass m^* and Seebeck coefficient can be expressed as [16,17]:

$$m_d^* = \frac{h^2}{2k_B T}\left(\frac{n}{4\pi F_{\frac{1}{2}}(\xi_F)}\right)^{\frac{2}{3}} \quad (2)$$

$$S = \frac{k_B}{e}\left[\frac{(\lambda+2)F_{\lambda+1}(\xi_F)}{(\lambda+1)F_\lambda(\xi_F)} - \xi_F\right] \quad (3)$$

with Fermi integral of order i

$$F_i(\xi_F) = \int_0^\infty \frac{x^i}{1 + e^{(x-\xi_F)}}dx \quad (4)$$

where h and ξ_F are the Planck constant and the reduced Fermi level $F_f/(k_BT)$, respectively. In our calculation, we assume that acoustic scattering is dominant in the composite samples and obtained a density of state effective mass m^* of 0.78 m_e, in good agreement with the reported result ($m^* = 0.75$ m_e) [7]. On the other hand, a slight increase in S of sample 1 mol% SnTe/$Ag_{0.005}Sn_{0.995}Se$ appears probably due to the energy filtering effect (EFE) caused by the incorporation of SnTe nanoparticles. To manifest EFE, we calculated the scattering parameter λ (see Table S1) that is usually related with the relaxation time τ by the relation: $\tau = \tau_0 E^{\lambda - 1/2}$, where E is energy of carriers and τ_0 is energy-independent constant. One can see that increased λ (~0.16) of the composite sample 1 mol% SnTe/

$Ag_{0.005}Sn_{0.995}Se$ leads to ~12 μV/K rise in *S*.

Fig. 5(c) shows *PF* of the samples *f* mol% SnTe/$Ag_{0.005}Sn_{0.995}Se$ ($f = 0$, 0.5, 1 and 1.5) as a function of temperature. At low temperatures (300 K–650 K), *PF* decrease monotonously with increasing *f* resulting from the large increase in electrical resistivity. Moreover, local maximum PF (at 300–500 K) decrease from 7.8 μW/cmK^2 to 6.0 μW/cmK^2, 5.0 μW/cmK^2 and 4.6 μW/cmK^2, as *f* increase from 0 to 0.5, 1 and 1.5, respectively. On the other hand, the maximum PF of 10.3 μW/cmK^2 is achieved at 875 K in the composite sample 0.5 mol% SnTe/$Ag_{0.005}Sn_{0.995}Se$. This enhancement of *PF* for 0.5 mol% SnTe/$Ag_{0.005}Sn_{0.995}Se$ comes mainly from the increase of both mobility μ and *S* at elevated temperatures.

3.3. Thermal conductivity and thermoelectric performance

The specific heat capacity C_p of the matrix was taken from Chen et al. [7] and the specific heat capacity C_p of SnTe was determined by:

$$C_p = C_{p,300} + C_{pT} \times \left((T/300)^{\alpha} - 1\right)/\left((T/300)^{\alpha} + C_{pT}/C_{p,300}\right) \quad (5)$$

where *T* is the absolute temperature and $C_{p,300}$ is the specific heat capacity at 300 K. For SnTe, $C_{p,300}$ is 0.197 Jg^{-1}K^{-1}, C_{pT} is 0.115 Jg^{-1}K^{-1}, and α is 0.63 [18]. C_p of the composite sample (see Fig. S1) can be determined by the rule of mixture:

$$C_P = (1-\chi)C_{P1} + \chi C_{P2} \quad (6)$$

with the mass fraction

$$\chi = \frac{f*M_1}{f*M_1 + (1-f)*M_2} \quad (7)$$

where C_p, C_{p1}, and C_{p2} are the specific heat for the composite sample, $Ag_{0.005}Sn_{0.995}Se$ and SnTe, respectively. M_1 and M_2 are the molar mass for $Ag_{0.005}Sn_{0.995}Se$ and SnTe. Due to the small proportion of SnTe nanoinclusions, the obtained value of C_p is similar to C_{p1}. Combining the thermal diffusivity *D*, the density *d* and specific heat C_p, one can calculate the total thermal conductivity based on $\kappa_{tot} = DdC_p$, as shown in Fig. 6. Clearly, total thermal conductivity for all the samples decrease with increasing temperature (300 K–750 K), suggesting the enhanced Umklapp process. Moreover, total thermal conductivity for the samples *f* mol% SnTe/$Ag_{0.005}Sn_{0.995}Se$ ($f = 0$, 0.5 and 1) decrease substantially with increasing content of SnTe above 350 K, which could be due to the enhanced phonons scattering. For composite samples *f* mol% SnTe/$Ag_{0.005}Sn_{0.995}Se$ ($f = 0.5$ and 1), total thermal conductivity is much lower than that of pristine $Ag_{0.005}Sn_{0.995}Se$. Specially, the total thermal conductivity for the composite sample with $f = 1$ reaches ~0.46 W/mK at 875 K, a reduction of ~13% as compared to that of pristine $Ag_{0.005}Sn_{0.995}Se$. Based on the Wiedemann-Franz-Lorenz relation, the electrical thermal conductivity is estimated by $\kappa_e = L_0T/\rho$, where L_0, ρ and *T* are the Lorenz number, the resistivity and the absolute temperature, respectively. The lattice thermal conductivity in the inset of Fig. 6 is deduced from the simple relation: $\kappa_l = \kappa_{tot} - \kappa_e$. Here, we calculated Lorenz number $L_0 \sim 1.5 \times 10^{-8}$V^{2}K^{-2} (see Table S1) using the formula (8) based on the assumption of transport dominated by acoustic phonon scattering mechanism and a single parabolic band [19]:

$$L = \left(\frac{k_B}{e}\right)^2 \frac{3F_0(\xi_F)F_2(\xi_F) - 4F_1(\xi_F)^2}{F_0(\xi_F)^2} \quad (8)$$

As far as we know, the lattice thermal conductivity for polycrystalline SnSe [7,8] is much higher than that (~0.2 W/mK along the *a* direction, ~0.3 W/mK along the *c* direction and ~0.35 W/mK along the *b* direction at 875 K) of single crystal SnSe [4]. However, as shown in the inset of Fig. 6, for the composite sample 0.5 mol% SnTe/$Ag_{0.005}Sn_{0.995}Se$, the lattice thermal conductivity at 875 K is ~0.38 W/mK, which is slightly higher than that (~0.35 W/mK) of single crystal SnSe along the *b* direction. Moreover, the lowest lattice thermal conductivity for 1 mol% SnTe/$Ag_{0.005}Sn_{0.995}Se$ at 890 K reduces ~16% as compared with that of pristine $Ag_{0.005}Sn_{0.995}Se$, which could be attributed to the enhanced phonon scattering due to the incorporation of SnTe nanoparticles. On the other hand, according to the Callaway mode, the lattice thermal conductivity can be treated as the cumulative contribution of phonons varying in frequency from 0 to the upper limit via [20]:

$$\kappa_l = \frac{4\pi k_B^4 T^3}{\nu h^3} \int_0^{\frac{\theta_D}{T}} \tau(\xi) \frac{\xi^4 e^{\xi}}{(e^{\xi}-1)^2} d\xi \quad (9)$$

where ν, *h*, θ_D, τ and ξ are the average phonon velocity, plank constant, Debye temperature, phonon relaxation time and the reduced phonon energy, respectively. Furthermore, phonon relaxation time τ is a variable related to different scattering mechanisms and can be expressed as:

$$\tau^{-1} = \tau_{PD}^{-1} + \tau_{NP}^{-1} + \tau_{P-P}^{-1} + \tau_{IF}^{-1} \quad (10)$$

where, τ_{PD}, τ_{NP}, $\tau_{P\text{-}P}$ and τ_{IF} are the relaxation time corresponding to scattering from point defect, nanoparticles, phonon-phonon interactions and interfaces, respectively. Clearly, these reductions in lattice thermal conductivity should be ascribed to stronger phonon scattering by point defect (τ_{PD}) of doped Ag, the incorporated nanoparticles (τ_{NP}) and the phase boundaries (τ_{IF}).

Fig. 7 depicts *ZT* values for all the samples as a function of temperature. High *ZT* value close to 1.6 of the matrix $Ag_{0.005}Sn_{0.995}Se$ could be due to highly oriented crystal grains along the (400) plane, which is slightly inferior to single crystal SnSe along the *b* direction [4]. On the other hand, by incorporating SnTe nanoparticles into the matrix $Ag_{0.005}Sn_{0.995}Se$, a largest *ZT* value of 1.6 ± 0.2 is obtained at 875 K for the composite sample 0.5 mol% SnTe/$Ag_{0.005}Sn_{0.995}Se$. One can see that *ZT* values in this work are

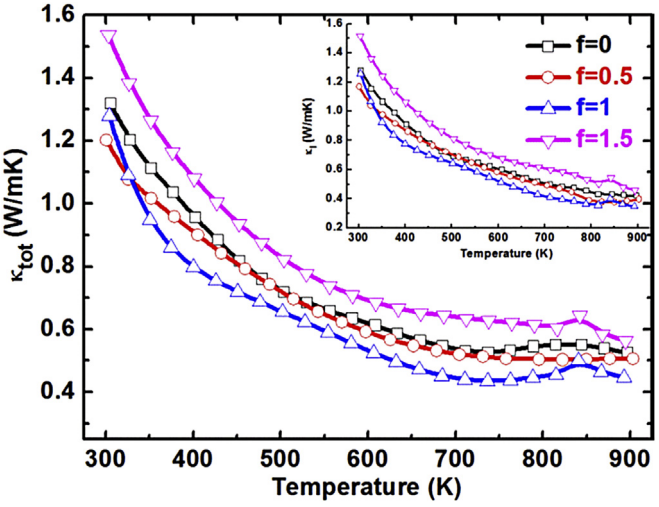

Fig. 6. Total thermal conductivity (lattice thermal conductivity in the inset) as a function of temperature for SPS synthesized bulk samples *f* mol% SnTe/$Ag_{0.005}Sn_{0.995}Se$ ($f = 0$, 0.5, 1 and 1.5).

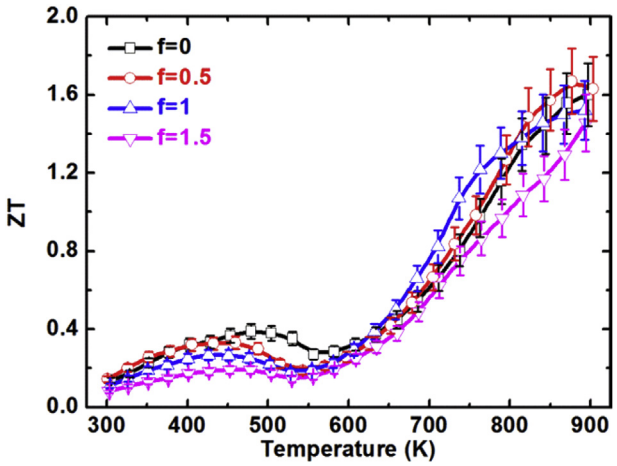

Fig. 7. *ZT* as a function of temperature for SPS synthesized bulk samples *f* mol% SnTe/$Ag_{0.005}Sn_{0.995}Se$ ($f = 0$, 0.5, 1 and 1.5).

superior to those of polycrystalline samples in previously studies [7,8]. The enhancement of *ZT* value for the composite sample 0.5 mol% SnTe/$Ag_{0.005}Sn_{0.995}Se$ benefits mainly from the increased *PF* (~10.3 μW/cmK^2) and reduced lattice thermal conductivity (~0.38 W/mK). In addition, highly oriented polycrystalline composite sample 0.5 mol% SnTe/$Ag_{0.005}Sn_{0.995}Se$ shows good experimental repeatability for this high *ZT*, as evidenced by measurements on four samples prepared independently (see Fig. S2). Present results indicate that proper incorporation of nanophase SnTe in $Ag_{0.005}Sn_{0.995}Se$ matrix can effectively enhance thermoelectric performance of the $Ag_{0.005}Sn_{0.995}Se$ based composite system.

4. Conclusions

In summary, highly oriented polycrystalline samples *f* mol% SnTe/$Ag_{0.005}Sn_{0.995}Se$ ($f = 0$, 0.5, 1 and 1.5) were synthesized by solid state melting and SPS method, and then thermoelectric properties were studied in the temperature range of 300 K–900 K. Firstly, highly preferred orientation along the (400) plane make the matrix $Ag_{0.005}Sn_{0.995}Se$ have high *ZT* value. Moreover, by incorporating 0.5 mol% SnTe nanoparticles into $Ag_{0.005}Sn_{0.995}Se$ matrix, power factor was slightly enhanced and meanwhile lattice thermal conductivity was reduced due to the enhanced interface phonon scattering. As a result, a largest *ZT* value of 1.6 ± 0.2 is achieved at 875 K for composite sample 0.5 mol% SnTe/$Ag_{0.005}Sn_{0.995}Se$, which indicates that incorporation of nanophase SnTe could effectively enhance thermoelectric performance of $Ag_{0.005}Sn_{0.995}Se$ based composite system. Furthermore, highly oriented polycrystalline composite sample 0.5 mol% SnTe/$Ag_{0.005}Sn_{0.995}Se$ shows good experimental repeatability for this high *ZT*. Therefore, the findings in this work will help to optimize thermoelectric performance of polycrystalline SnSe based system, which make it be a promising candidate for power generation.

Acknowledgements

Financial support from National Natural Science Foundation of China (No. 11374306) was gratefully acknowledged.

Appendix A. Supplementary data

Supplementary data related to this article can be found at http://dx.doi.org/10.1016/j.jallcom.2016.07.291.

References

[1] J.P. Heremans, V. Jovovic, E.S. Toberer, A. Saramat, K. Kurosaki, A. Charoenphakdee, S. Yamanaka, G.J. Snyder, Science 321 (2008) 554.
[2] C.M. Jaworski, B. Wiendlocha, V. Jovovic, J.P. Heremans, Energy Environ. Sci. 4 (2011) 4155.
[3] K.F. Hsu, S. Loo, F. Guo, W. Chen, J.S. Dyck, C. Uher, T. Hogan, E.K. Polychroniadis, M.G. Kanatzidis, Science 303 (2004) 818.
[4] L.D. Zhao, S.H. Lo, Y.S. Zhang, H. Sun, G.J. Tan, C. Uher, C. Wolverton, V.P. Dravid, M.G. Kanatzidis, Nature (2014) 508.
[5] K.L. Peng, X. Lu, H. Zhan, S. Hui, X.D. Tang, G.W. Wang, J.Y. Dai, C. Uher, G.Y. Wang, X.Y. Zhou, Energy Environ. Sci. 9 (2016) 454–460.
[6] L.D. Zhao, G.J. Tan, S.Q. Hao, J.Q. He, Y.L. Pei, H. Chi, H. Wang, S.K. Gong, H.B. Xu, V.P. Dravid, C. Uher, G.J. Snyder, C. Wolverton, M.G. Kanatzidis, Science 1 (2016) 351.
[7] C.L. Chen, H. Wang, Y.Y. Chen, T. Day, G.J. Snyder, J. Mater. Chem. A 2 (2014) 11171–11176.
[8] T.R. Wei, C.F. Wu, X.Z. Zhang, Q. Tan, L. Sun, Y. Pan, J.F. Li, Phys. Chem. Chem. Phys. 17 (2015) 30102–30109.
[9] K. Biswas, J.Q. He, G.Y. Wang, S.H. Lo, C. Uher, V.P. Dravid, M.G. Kanatzidis, Energy Environ. Sci. 4 (2011) 4675–4684.
[10] K. Biswas, J.Q. He, Q.C. Zhang, G.Y. Wang, C. Uher, V.P. Dravid, M.G. Kanatzidis, Nat. Chem. 3 (2011) 160–166.
[11] J.H. Li, Q. Tan, J.F. Li, D.W. Liu, F. Li, Z.Y. Li, M.M. Zou, K. Wang, Adv. Funct. Mater. 23 (35) (2013) 4317–4323.
[12] T.H. Zou, X.Y. Qin, D. Li, G.L. Sun, Y.C. Dou, Q.Q. Wang, B.J. Ren, J. Zhang, H.X. Xin, Y.Y. Li, Appl. Phys. Lett. 104 (2014) 013904.
[13] G.J. Tan, L.D. Zhao, F.Y. Shi, J.W. Doak, S.H. Lo, H. Sun, C. Wolverton, V.P. Dravid, C. Uher, M.G. Kanatzidis, J. Am. Chem. Soc. 136 (19) (2014) 7006–7017.
[14] M. Zhou, Z.M. Gibbs, H. Wang, Y.M. Han, C.N. Xin, L.F. Li, G.J. Snyder, Phys. Chem. Chem. Phys. 16 (2014) 20741.
[15] Q.Q. Wang, X.Y. Qin, D. Li, J. Appl. Phys. 113 (2013) 124901.
[16] Y.Y. Li, D. Li, X.Y. Qin, X.H. Yang, Y.F. Liu, J. Zhang, Y.C. Dou, C.J. Song, H.X. Xin, J. Mater. Chem. C 4 (2015) 1039.
[17] T.H. Zou, X.Y. Qin, D. Li, J. Appl. Phys. 115 (2014) 053710.
[18] M. Wagner, These de doctorat, Universität Wien, 2007.
[19] E.S. Toberer, P. Rauwel, S. Gariel, J. Tafto, G.J. Snyder, J. Mater. Chem. 20 (2010) 9877.
[20] Y.B. Luo, J.Y. Yang, M. Liu, Y. Xiao, L.W. Fu, W.X. Li, D. Zhang, M.Y. Zhang, Y.D. Cheng, J. Mater. Chem. A 3 (2015) 1251.